

3D Reconstruction from Multimodal and Coaxial Camera Rigs Using Image Correspondences Derived from Perceived Motion

Paper ID ****< replace **** here and in header with paperID>

Abstract

3D reconstruction from image pairs taken from different camera perspectives relies on finding corresponding points between the images and using those corresponding points to estimate a dense disparity map. Today's correspondence finding algorithms primarily use image features or pixel intensities common between image pairs. Some 3D computer vision applications, however, don't produce the desired results using correspondences derived from image features or pixel intensities. Two examples are the multimodal camera rig and the center region of a coaxial camera rig. In this paper we present a 3D reconstruction technique using a novel automatic correspondence finding algorithm that aligns image sequences using optical flow fields. Our method applies to applications where there is inherent motion between the camera rig and the scene and where the scene has enough visual texture to produce optical flow. We apply the technique to a traditional binocular stereo rig consisting of an RGB/IR camera pair and to a coaxial camera rig. We present results for synthetic flow fields and for real images sequences.

1. Introduction

Finding corresponding points in image pairs taken from two different perspectives is one of the most active areas of research in computer vision [10, 18, 20]. It forms the basis of 3D reconstruction as well as being a critical component of many other computer vision and image processing applications that require pixel by pixel alignment between image pairs [9, 26].

Existing correspondence finding techniques are based on matching pixel intensity values or features which are derived from pixel intensity values. This, in turn, allows the estimation of dense disparity maps which, given the camera geometry, allows the estimation of dense depth maps. Where image registration is the ultimate goal, the correspondences provide the geometrical transformations that allows one image, the sensed image, to be transformed into the second image, the reference image.

There are computer vision applications, however, where

traditional correspondence finding techniques do not produce the desired results. Two notably cases are multimodal camera rigs where the images produced from different sensor types are not similar enough to be aligned using pixel intensities or features [26] and the center region of a coaxial camera rig [17] where the disparity is too small to produce good triangulation. There are also multi-camera applications where it is desirable to augment the use of pixel intensities and/or image features to improve the finding of intra-camera correspondences.

In this paper we introduce a novel automated method for finding correspondences using the optical flow fields from two cameras. We apply the technique to images acquired by a multimodal stereo rig where one camera contains an RGB sensor and the other camera contains an IR sensor, as well as to a coaxial camera rig. In applications where there is sufficient motion between the camera rig and the scene (scanning security camera, camera mounted on a vehicle, endoscope, etc.) and where the scene exhibits enough texture to produce optical flow, our method finds correspondences between multi-view image sequences without using intra-camera pixel intensities or features. From these correspondences we estimate dense disparity maps with accuracies similar to, and in certain cases, substantially better than, techniques that align images based on image features or pixel intensities.

2. Related Work

2.1. Multimodal Binocular Stereo

Aligning images from stereo rigs consisting of cameras with multimodal sensors has been an active research area for the last decade and a half. Initially inspired by the work done to match medical images to models [23] it has more recently been motivated by the need for surveillance systems that use a combination of visible light and infrared cameras to detect targets. As noted by Yaman and Kalkan [24], traditional image alignment techniques used in stereo vision are not applicable to multimodal camera rigs because the pixel intensities can be substantially different in a visible light image vs. an IR image. Solutions to the multimodal problem fall into two

broad categories. The first uses Mutual Information (MI). MI was originally proposed by Viola and Wells [23] to match medical images to models. To our knowledge, Egnal [5] was the first to use MI as a similarity measure to match multimodal stereo images. Since then, numerous improvements have been made including adaptive windowing [6], incorporating prior probabilities [7], regions of interest [12-14], and extending MI using gradient information [4].

More recently, local self similarity (LSS), originally used in template matching, was proposed for use in a multimodal camera rig [21]. Most recently Yaman and Kalkan [24] used MI to generate dense disparity maps from multimodal camera rigs.

The method we present avoids using visual similarity measures between the images from the two different sensor types by computing the optical flow fields from the two sensors and then aligning the flow fields. This permits images with no common features to be aligned as long as there is motion between the camera and the scene and the scene has enough texture to produce optical flow.

Verri and Poggio [22] have shown that in many cases optical flow is not equivalent to the motion field. While optical flow algorithms have improved substantially since the Verri and Poggio paper (see [19] and [3] for summaries of the progression of optical flow algorithm development); optical flow errors caused by the aperture problem, non-Lambertian surfaces, and non-uniform changing illumination, still exist.

For finding image correspondences, however, the optical flow fields do not need to be equivalent to the motion fields. For example, errors caused by the aperture problem where only the motion tangential to edges is detected or errors caused by moving shadows, will be perceived by the two sensors identically and alignment is unaffected. The primary requirement is that the optical flow computation be invariant to different light wavelengths.

2.2. Depth from Zooming - Coaxial Camera

Depth from images taken at different focal lengths along a common optical axis was first proposed by Ma and Olsen [17]. Lavest et al. [16, 15] provide a proof for inferring 3D data from images taken at multiple focal lengths and models a revolving object. Asada et al. [1] and Baba et al. [2] present a method for doing 3D reconstruction using blur from zoom. Gao et al. [8] present a distance measurement system for mobile robots using zooming. Most recently, Zhang and Qi [25] describe a method for 3D reconstruction from multi-focal length images using a snake-search algorithm.

The primary reason researchers have focused on using a single camera at different focal lengths to do 3D reconstruction has been cost. However, there are several

other advantages. Ma and Olsen alluded to the fact that a depth from zoom camera exhibits substantially smaller occlusions than an equivalent binocular stereo camera rig. Additionally, there are applications where a stereo baseline is prohibitive (endoscope or bore scope) and where the known correspondence point on the optical axis is an advantage to image registration. Finally, where image registration is the ultimate objective of the application (e.g. alignment of images from two different types of sensors without attempting 3D reconstruction), a coaxial camera produces substantially smaller disparity errors than a binocular stereo rig.

The coaxial camera rig [11] is equivalent to simultaneous depth from zooming, but instead of changing the focal length of a single fixed camera, two cameras are arranged such that the cameras form images along the same optical axis. This is done by splitting the optical path with a beam splitter and aligning the two cameras such that their optical centers image the same point in the 3D scene. The coaxial camera rig combined with image correspondences derived from perceived motion overcomes the two main problems of depth from zooming. First, simultaneous images taken at two different focal lengths overcomes the stationary scene constraint of depth from zooming. Second, using the flow field to align image pairs overcomes the unrecoverable point problem in the center region described by Ma and Olsen. This later advantage is due to the depth estimate being derived from the ratio of the flow fields taken at different focal lengths as opposed to the extremely small disparities found in the center region of a coaxial camera rig.

3. Variational Models

3.1. Binocular Stereo

Referring to Figure 1, let $\bar{x}_l := (x_l, y_l)^T$, $\bar{x}_r := (x_r, y_r)^T$ represent points in the image domain of the left and right cameras. Let $\bar{h}(\bar{x}) :=$ the disparity between \bar{x}_l and \bar{x}_r such that \bar{x}_l and $\bar{x}_r + \bar{h}(\bar{x}_r)$ represent the same point $\bar{X}(\bar{x}_l) := (X, Y)$ in the scene. Let $f :=$ the focal lengths of the cameras and $Z_0(\bar{x}_l), Z_1(\bar{x}_l) :=$ the distance between the optical center of the left camera and a point in the scene correspond to \bar{x}_l at time = 0 and 1, the distance being measured along the optical axis. $\Delta Z(\bar{x}_l)$ is then the difference in Z between the time = 1 and time = 0. $\bar{X} :=$ the distance from the optical axis to a point in the scene and $\Delta \bar{X} :=$ the change in the distance from the optical axis between time = 0 and time = 1. $b :=$ the stereo baseline. $\bar{w}_l, \bar{w}_r :=$ the ideal flow fields in the left and right cameras.

The relationship between an ideal flow field in the two cameras is:

$$p(\bar{x}_l)w_l(\bar{x}_l) = w_r(\bar{x}_l + h(\bar{x}_l)) \quad (1)$$

where:

$$p(\bar{x}_l) = 1 + \frac{\Delta Z(\bar{x}_l)h(\bar{x}_l)}{f\Delta\bar{X} - \Delta Z(\bar{x}_l)\bar{x}_l} \quad (2)$$

$p(\bar{x}_l)$ has a direct physical interpretation. From equation (2) it can be seen that $p(\bar{x}_l) = 1$ if $\Delta Z(\bar{x}_f) = 0$. Referring to Figure 1, one can see that a change in Z introduces a slight parallax (ρ) in the finishing points of the optical flow detected by the two cameras. $p(\bar{x}_l)$ compensates for the parallax and can be solved for directly from the coaxial camera geometrically.

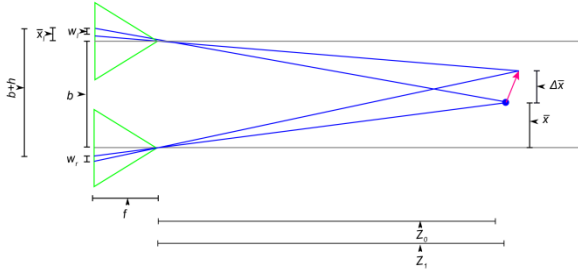


Figure 1: Binocular stereo camera rig geometry.

The first term in our stereo variational model is an optical flow matching term:

$$E_{match} = \int_a^b \frac{1}{2} [p(\bar{x}_l)w_l(\bar{x}_l) - w_r(\bar{x}_l + h(\bar{x}_l))]^2 dx \quad (3)$$

The second term is a smoothness term:

$$E_{smooth} = \frac{1}{2} \int_a^b \|\nabla Z(\bar{x}_l)\|^2 dx \quad (4)$$

The total energy that we want to minimize is:

$$E_{total} = \gamma E_{match} + \alpha E_{smooth} \quad (5)$$

where γ and α are tuning constants.

3.2. Coaxial Camera

Referring to Figure 2, let $\bar{x}_f := (x_f, y_f)^T$, $\bar{x}_b := (x_b, y_b)^T$ represent points in the image domain of the front and back cameras. Let $\bar{h}(\bar{x}) :=$ the disparity between \bar{x}_f and \bar{x}_b such that \bar{x}_f and $\bar{x}_b - \bar{h}(\bar{x}_f)$ represent the same point $\bar{X}(\bar{x}_f) := (X, Y)$ in the scene. Let $f_f, f_b :=$ the focal lengths for the front camera and back camera and $Z(\bar{x}_f) :=$ the distance between the optical center of the front camera and a point in the scene corresponding to \bar{x}_f , the distance being measured along the optical axis. $b :=$ the distance between the optical center of the two cameras.

$\bar{w}_f, \bar{w}_b :=$ the ideal flow fields in the front and back cameras.

The relationship between an ideal flow field in the two cameras is:

$$m(\bar{x}_f)w_f(\bar{x}_f) = c(\bar{x}_f)w_b(\bar{x}_f m(\bar{x}_f)) \quad (6)$$

where:

$$m(\bar{x}_f) = \left(\frac{f_b}{f_f} \right) \left(\frac{Z(\bar{x}_f)}{Z(\bar{x}_f) + b} \right) \quad (7)$$

and

$$c(\bar{x}_f) = \left(\frac{w_f(\bar{x}_f)}{\left(\frac{Z_0(\bar{x}_f) + b}{Z_1(\bar{x}_f) + b} \right) \left(\frac{Z_1(\bar{x}_f)}{Z_0(\bar{x}_f)} \right) (w_f(\bar{x}_f) + \bar{x}_f) - \bar{x}_f} \right) \quad (8)$$

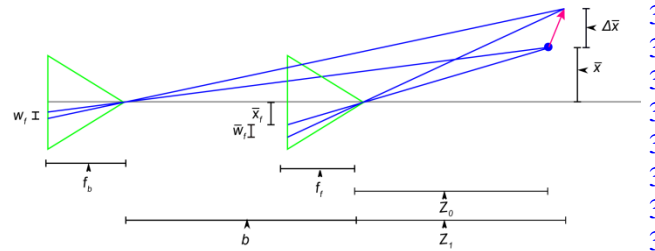


Figure 2: Coaxial camera rig geometry.

Where $Z_0(\bar{x}_f)$ and $Z_1(\bar{x}_f)$ are Z at time = 0 and time = 1.

Like $p(\bar{x}_l)$ in the binocular stereo example, $c(\bar{x}_f)$ has a direct physical interpretation. From equation 5 it can be seen that $c(\bar{x}_f) = 1$ if $Z_0(\bar{x}_f) = Z_1(\bar{x}_f)$ or when $\Delta Z(\bar{x}_f) = 0$. Referring to Figure 3 one can see that a change in Z introduces a slight parallax (ρ) in the finishing points of the optical flow detected by the two cameras. $c(\bar{x}_f)$ compensates for the parallax and can also be solved for directly from the coaxial camera geometrically.

The first term in our coaxial camera variational model is an optical flow matching term:

$$E_{match} = \int_a^b \frac{1}{2} [m(\bar{x}_f)w_f(\bar{x}_f) - c(\bar{x}_f)w_b(\bar{x}_f m(\bar{x}_f))]^2 dx \quad (9)$$

The second term is a smoothness term:

$$E_{smooth} = \frac{1}{2} \int_a^b \|\nabla Z(\bar{x}_f)\|^2 dx \quad (10)$$

The total energy that we want to minimize is:

$$E_{total} = \gamma E_{match} + \alpha E_{smooth} \quad (11)$$

where γ and α are tuning constants.

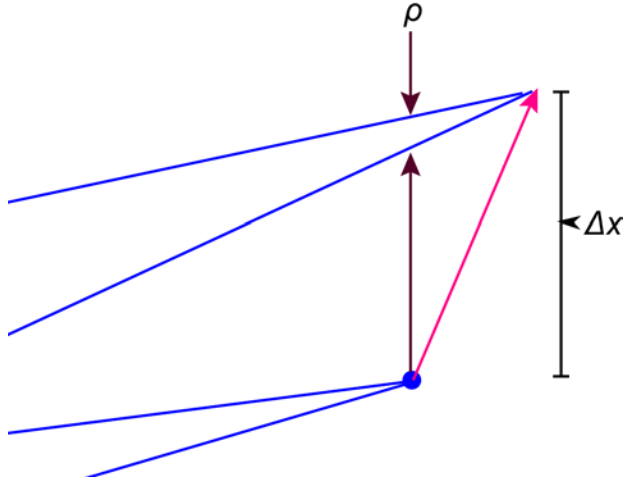


Figure 3: Parallax caused by ΔZ in a coaxial camera rig.

4. Numerical Solution

4.1. Euler-Lagrange

The Euler-Lagrange equations for (3), (4), (9), and (10) are taken with respect to z . The solutions are straightforward and are not presented here.

We reduce the problem to a 1D optimization problem by observing that the solutions for the stereo camera rig lie on horizontal epipolar lines and for the coaxial camera rig the solutions lie on radial epipolar lines. For the coaxial camera rig, we resample the front and back images onto polar coordinates. In both cases the Euler-Lagrange equations (one for the x direction and one for the y direction) are solved using the gradient decent method.

4.2. Initialization

For the first iteration, we need an initial estimate for Z_0 . While it's possible to solve for Z_0 and Z_1 simultaneously the best results are obtained if the first image pair only contains ΔX or only ΔZ translation. In this case either $Z_0 = Z_1$ or $\bar{X}_0 = \bar{X}_1$ and the initial estimate is significantly simplified.

For a stereo camera rig and a scene without an occlusion in the center region there exists a pixel pair on each epipolar line where $\bar{x}_l = -\bar{x}_r$. These pixel pairs represent stereo correspondences and can be used to derive an initial estimate for Z using the standard stereo equation. The optical flow can then be used to estimate the depth map along each epipolar line.

For a coaxial camera, an initial Z estimate can be made by observing that when an optical flow vector ends on the optical axis we have a special case where:

$$w_f(\bar{x}_f) = \bar{x}_f \quad (12)$$

The initial Z value can then be found using (13):

$$Z(\bar{x}_f = (0,0)^T) = \frac{b}{\frac{w_f(0)f_b}{w_b(0)f_f} - 1} \quad (13)$$

As in the stereo configuration, we use the optical flow to make a Z estimate along each epipolar line.

4.3. Stopping Criteria

We used one of two stopping criteria depending on the quality of the flow fields and the value chosen for α . When the flow fields closely represent the motion fields and α is small (minimal Z smoothing), we use the error in the first term of the energy equation, which represents the mismatch in registration of the two flow fields, and stop when this number becomes suitably small.

Where the flow fields are noisy and not as good a representation of the motion field we need to increase α to get good results. With more substantial smoothing, the smoothing term can pull the Z estimate away from the correct value if γ is large and/or if many iterations are performed. In this case we stopped the iterations when the smoothing term was approximately equal to, but of opposite sign to the flow matching term. This later approach often results in slightly larger errors in the first term of the energy equation, but our experiments suggest that it improves the accuracy of the disparity estimations because we stop iterating before the smoothness term pulls the estimate too far from the ideal solution.

5. Experiments

5.1. Synthetic optical flow field

For the synthetic optical flow fields we defined the geometry of a 3D scene and project the 3D motion of that scene onto a virtual image plane via an ideal pinhole camera model. This results in a simulated optical flow field that is exactly equal to the motion field. The simulated flow field experiments provide an estimate of the upper boundary of accuracy for our methodology and expose limitations on the 3D velocity with respect to the camera geometry.

Stereo Camera Rig. To determine the accuracy of the resulting image alignment we reconstruct the depth map along a horizontal epipolar line using the results of registration and compare the reconstructed depth map with

the original scene geometry computing both the RMS disparity error and the resulting RMS depth error.

For our synthetic flow images we created a scene geometry that ranges from 10 m to 20 m from the camera center. $f = 4.0$ mm, the cameras have .006 mm square pixels, velocity in the XY plane was varied from 0.5 m/s to 3.5 m/s and velocity along the Z-axis ranged from 2.5 m/s toward the camera to 2.5 m/s away from the camera. The camera frame rate was set to 30 fps. We set $\gamma = 1 \cdot 10^9$ and $\alpha = 1 \cdot 10^{-1}$.

Figures 4 and 5 show the results for a smooth scene without any occlusions. The worst case RMS depth error is $< 0.25\%$ and worst case RMS disparity errors < 0.01 pixels. The accuracy is slightly reduced as delta Z increases and delta X decreases. We believe that this slight reduction in accuracy is due to the cancellation that occurs in the flow fields between X and Z translations in some areas of the image.

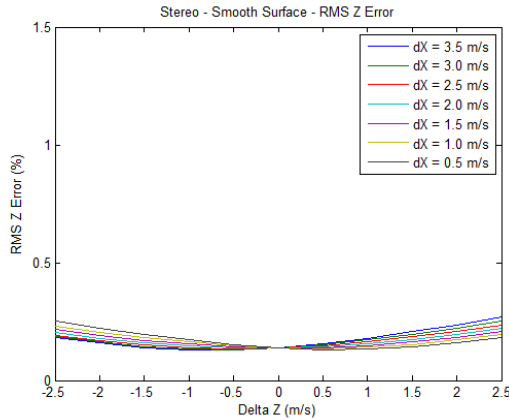


Figure 4: RMS Z error, multimodal stereo rig, synthetic images, smooth surface.

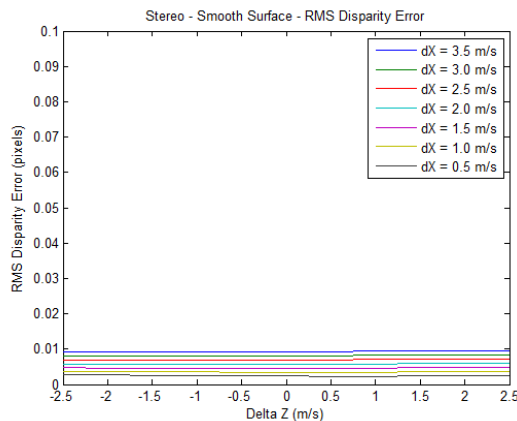


Figure 5: RMS disparity error, multimodal stereo rig, synthetic images, smooth surface.

error increases, but is still well within acceptable levels for most applications.

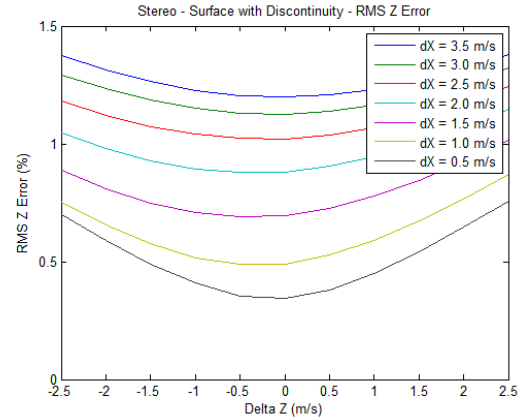


Figure 6: RMS Z error, multimodal stereo rig, synthetic images, surface with discontinuities.

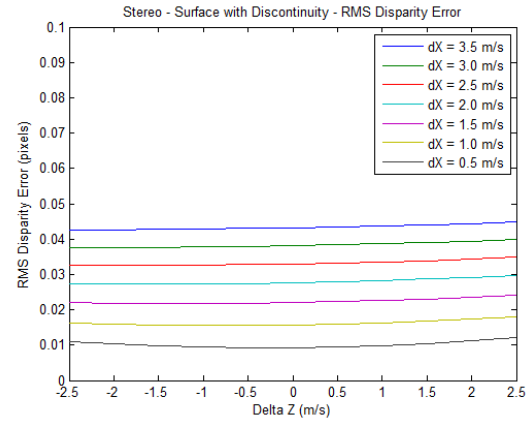


Figure 7: RMS disparity error, multimodal stereo rig, synthetic images, surface with discontinuities.

Coaxial Camera Rig. For the coaxial camera rig we determine the accuracy of the resulting image alignment by estimating the depth map along radial lines and comparing that to the original scene geometry by computing the RMS depth and disparity error.

For our synthetic flow images we used the same scene geometry as for the stereo camera rig. $f_i = 4.8$ mm, $f_b = 4.0$ mm, the camera has .002 mm square pixels, velocity in the XY plane was varied from 0.5 m/s to 3.5 m/s and velocity along the Z-axis ranged from 2.5 m/s toward the camera to 2.5 m/s away from the camera. The camera frame rate was set to 30fps. We set $\gamma = 1 \cdot 10^{11}$ and $\alpha = 5 \cdot 10^{-5}$.

Figures 8 and 9 show the results for a smooth scene for a horizontal line. With the exception of the slowest XY displacement (0.5 m/s) and highest Z displacements, RMS depth error is $< 0.15\%$. The shape of the curves suggest that there may be limitation on how large the Z

Figures 6 and 7 show the results for a scene with a large occlusion caused by a large (8 m) discontinuity. The RMS

displacement can be relative to the camera geometry and the XY displacement and still produce good results. We believe that this limitation may be due to cancellation which can occur between optical flow produced by lateral translation and the flow produced by forward translation in certain areas in the image.

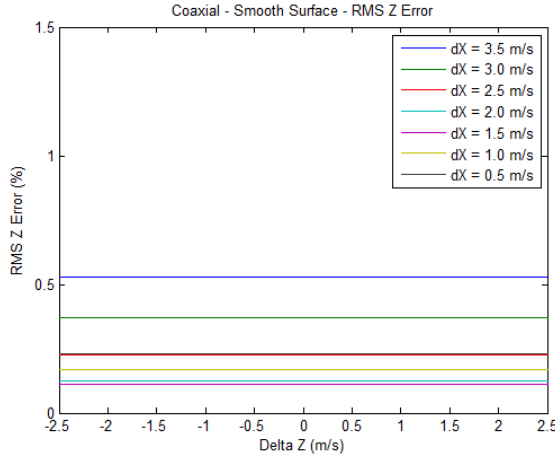


Figure 8: RMS Z error, coaxial camera rig, synthetic images, smooth surface.

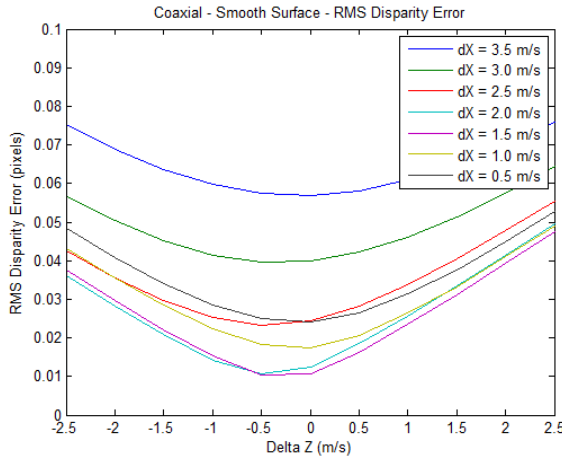


Figure 9: RMS disparity error, coaxial camera rig, synthetic images, smooth surface.

Figures 10 and 11 show the results for a scene with a large (8 m) discontinuity. The RMS error increases, but is still within acceptable levels for a wide range of applications.

5.2. Real Flow Fields

Stereo Camera Rig. Our multimodal stereo camera rig consists of one camera with an RGB sensor and a second camera with an IR sensor. The camera rig was mounted on a precision XY table and the camera rig was translated a known distance between frames. Accuracy was

determined by comparing the estimated camera rig displacement to the known camera rig displacement and converting to disparity.

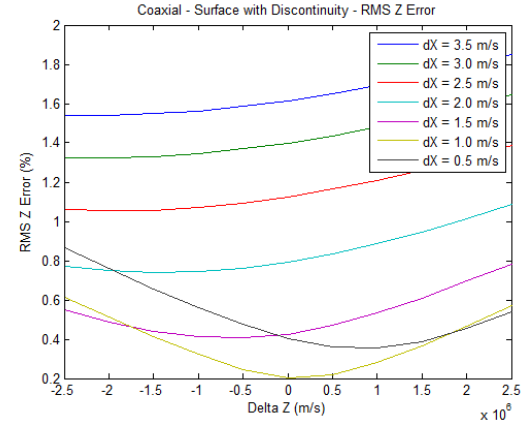


Figure 10: RMS Z error, coaxial camera rig, synthetic images, surface with discontinuities.

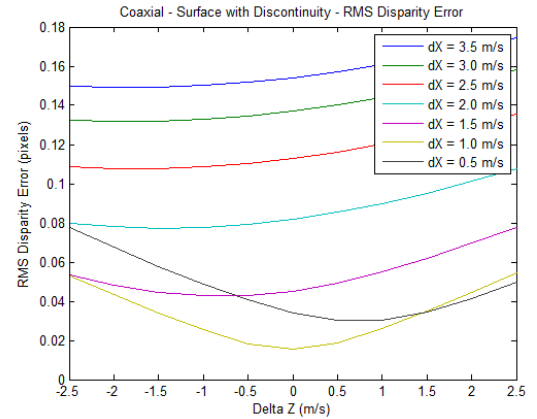


Figure 11: RMS Z disparity, coaxial camera rig, synthetic images, surface with discontinuities.

For the multimodal stereo camera, our scene is shown in Figure 12. There are small occlusions between the geometric shapes. Velocity in the XY plane was varied between 0.15 and 0.3 m/s, which when scaled to match our synthetic images would be about 4 m/s. The cameras in the stereo rig had 5.3 micron (IR) and 6 micron (RGB) square pixels and 7.0 mm (IR) and 7.7 mm (RGB) focal lengths. The images were corrected for the difference in pixel size and focal length. The baseline $b = 75$ mm. Gamma ranged from 0.2 to 0.5 and alpha was set at 0.01. To compute optical flow, we used the large scale optical flow algorithm from Brox and Malik [3].

Figure 13 shows the disparity errors and Figure 17 show a 3D rendering. At higher velocities the RMS disparity errors ranged from under 3 pixels to slightly over 8 pixels.

As the velocity drops the disparity error increases. We believe this is due to the errors in optical flow being higher as a percent of the flow for flow fields with smaller magnitudes. The results at higher lateral velocities compare very favorably to existing multimodal camera registration techniques.



Figure 12: Multimodal stereo rig scene.

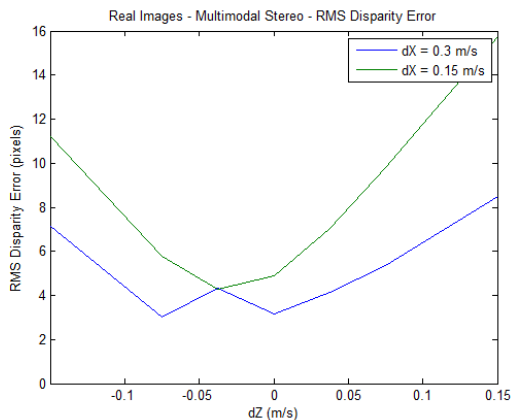


Figure 13: Disparity errors, real images, multimodal stereo camera rig.

Coaxial Camera Rig. The coaxial camera rig consists of a pair of cameras with RGB sensors on the same XY table described above. The camera arrangement is shown in Figure 14. Coaxial camera depth accuracy was also determined by estimating the camera movement using the estimated depth map and optical flow field and comparing the estimated camera rig displacement to the actual displacement.

Our scene (Figure 15) consisted of a 10 cm diameter by 17 cm tall cylinder located 75 cm from the optical center of the front camera in the camera rig and a planar background located 115 cm from the optical center of the front camera. There is a relatively large discontinuity between the cylinder and the planar background similar in

scale to that of our second set of synthetic experiments. Velocity in the XY plane was 0.3 m/s, which when scaled to match our synthetic images would be 4 m/s. The cameras in the coaxial rig have 0.006 mm square pixels, focal lengths of 7.7 mm and 5.8 mm (front and back respectively), and $b = 143.3$ mm. We set $\gamma = 2 \cdot 10^6$ and $\alpha = .05$. As with the stereo rig, we used the large scale optical flow algorithm from Brox and Malik.

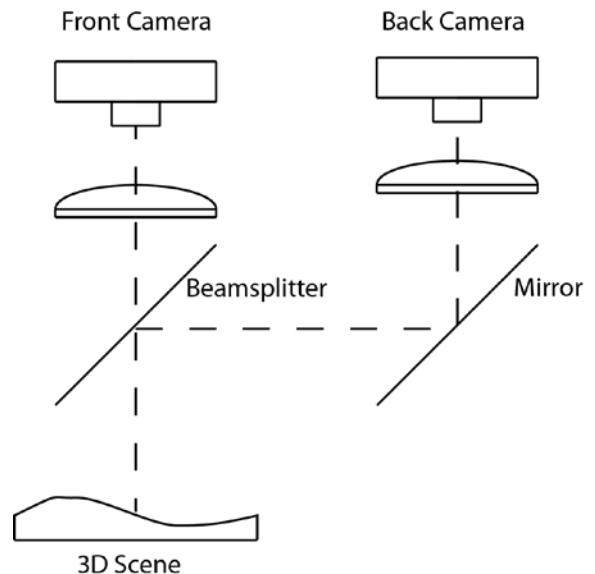


Figure 14: Coaxial camera rig..

Figure 16 shows the disparity errors and Figure 18 shows a 3D rendering. The RMS disparity error is typically less than 1% except where we get the cancellation in the flow fields between the forward translation and the lateral translation. While substantially better than the results from the stereo rig, a coaxial camera rig requires considerably smaller disparity errors to produce the same depth errors as a stereo rig. However, for applications where image alignment is the objective, these results suggest that a coaxial camera rig is superior to a stereo rig.

6. Conclusions

Our results provide solid evidence that it's possible to find image correspondence using the optical flow fields provided that there is sufficient motion between the camera and the scene and that the scene has sufficient texture to produce optical flow. One advantage of our method is that images that don't have common pixel intensities or features can be aligned. Another advantage is that highly accurate sub-pixel alignment is possible in the center region of a coaxial camera. Both cases permit the estimation of dense disparity maps which can be converted into dense depth maps for 3D reconstruction

and the relative velocity estimation between the scene and the camera rig.



Figure 15: Coaxial camera rig scene.

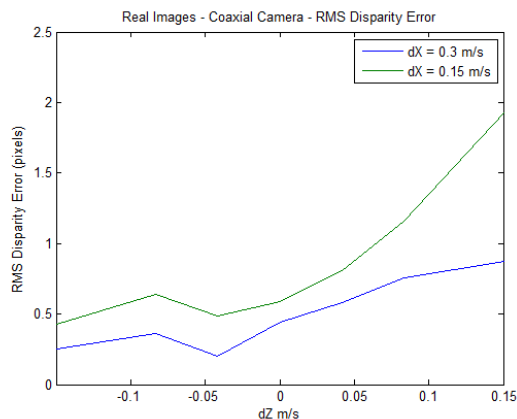


Figure 16: Disparity errors, real images, multimodal stereo camera rig.

With sufficient motion between the cameras and the scene and a scene that produces sufficient optical flow, our technique produces image alignment for a multimodal camera rig which is comparable to feature and pixel intensity based methods that align pairs of visible light images.

Our technique appears to be robust to flow fields that are not a good representation of the motion field as long as the flow fields in the two cameras reflect the same errors (e.g. the aperture problem and variation in illumination). This suggests that the intra-camera images might be used as an additional term in the optical flow computation (e.g. intra-camera image smoothing) to improve both the optical flow computation and the results intra-camera image alignment.

Our results suggest that our technique could produce good results on moving multimodal camera rig (scanning security camera or vehicle mounted camera) and for a coaxial camera rig, allow stereo reconstruction in

situations where a standard stereo baseline isn't feasible (e.g. endoscope or bore-scope).

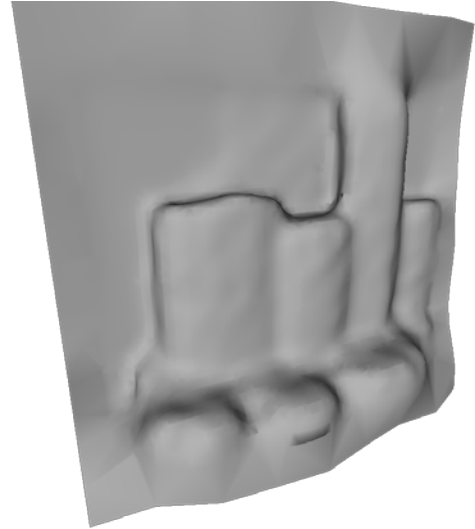


Figure 17: 3D Rendering from Multimodal Stereo Rig

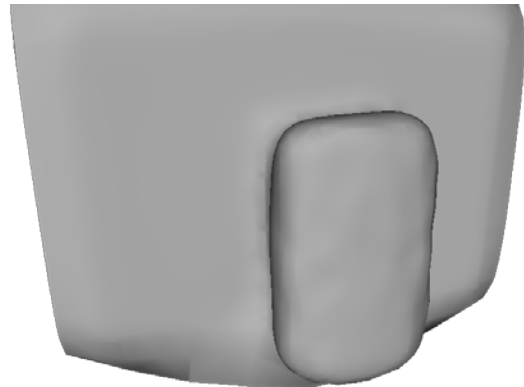


Figure 18: 3D Rendering from coaxial camera rig

References

- [1] N. Asada, m. Baba, and A. Oda, "Depth from Blur by Zooming," in *Proceedings of the Vision Interface Annual Conference*, Ottawa, Canada, 2001.
- [2] M. Baba, N. Asada, and T. Migita, "A Thin Lens Based Camera Model for Depth Estimation from Defocus and Translation by zooming," in *Proc. 15th International Conference on Vision Interface*, Calgary, Canada, 2002.
- [3] T. Brox and J. Malik, "Large Displacement Optical Flow Descriptor Matching in Variational Motion Estimation," *IEEE Transactions on Pattern Analysis and Machine Intelligence*, 2010.
- [4] F. B. Campo, R. L. Ruiz, and A. D. Sappa, "Multimodal Stereo Vision System: 3D Data Extraction and Algorithm Evaluation," *IEEE Journal*

- of *Selected Topics In Signal Processing*, vol. 6, no.5, 2012.
- [5] G. Egnal, "Mutual information as a Stereo Correspondence Measure," *Technical Report MS-CIS-00-20, Computer and Information Science, University of Pennsylvania, Philadelphia, USA*, 2000.
- [6] C. Fookes, A. Lamanna, and M. Bennamoun, "A new stereo image matching technique using mutual information," in *In Proceedings of the International Conference on Computer, Graphics and Imaging, CGIM'01, pages 168-173, Honolulu, USA, 2001. Iasted, ISBN 0-88986-303-2.*, 2001.
- [7] C. Fookes, S. Maeder, S. Sridharan, and J. Cook, "Multi-Spectral Stereo Image Matching using Mutual Information," in *Proceedings of the 2nd International Symposium on 3D Data Processing, Visualization, and Transmission*, 2004.
- [8] H. Gao, J. Liu, Y. Yu, and Y. Li, "Distance measurement of zooming image for a mobile robot," *International Journal of Control, Automation and Systems*, vol. 11, pp. 782-789, 2013.
- [9] A. A. Goshtasby, *Image registration principles tools methods*: Springer, 2012.
- [10] R. Hartly and A. Zisserman, *Multiple View Geometry in computer vision*: Cambridge University Press, 2003.
- [11] R. Kirby, "Three Dimensional Surface Mapping System Using Optical Flow US2013321790A1," USA Patent, 2012.
- [12] S. Krotosky and T. Mohan, "Registration of Multimodal Stereo Images using Disparity Voting from Correspondence Windows," in *IEEE Conf. on Advanced Video and Signal based Surveillance (AVSS'06)*, 2006.
- [13] S. Krotosky and M. Trivedi, "Multimodal Stereo Image Registration for Pedestrian Detection," in *in Proc. IEEE Intell. Transp. Syst. Conf., Sep. 2006, pp. 109-114*, 2006.
- [14] S. Krotosky and M. Trivedi, "Mutual information based registration of multimodal stereo videos for person tracking," *Computer Vision and Image Understanding*, vol. 106, pp. 270-287, 2007.
- [15] J. Lavest, G. Rives, and M. Dhome, "Three Dimensional Reconstruction by Zooming," *IEEE Transactions on Robotics and Automation*, vol. 9, pp. 196-207, 1993.
- [16] J. Lavest, G. Reves, and M. Dhome, "Modeling an Object of Revolution by Zooming," *IEEE Transactions on Robotics and Automation*, vol. VOL. II, NO. 2, April 1995, 1995.
- [17] J. Ma and S. I. Olsen, "Depth from Zooming," *J. Opt. Soc. Am. A* vol. 7, October 1990 1990.
- [18] D. Scharstein and R. Szeliski, "A taxonomy and evaluation of dense two frame stereo correspondance agorithms," in *IJCV*, 2001.
- [19] D. Scharstein, R. Szeliski, and R. Zabih, "A taxonomy and evaluation of dense two frame stereo correspondence algorithms," *International Journal of Computer Vision* vol. 47, pp. 7-42, 2002.
- [20] R. Szeliski, *Computer Vision. Algorithms and Applications*. New York: Springer, 2011.
- [21] A. Toraby and G. Bilodeau, "Local self-similarity as a dense stereo correspondence measure for themal visible video registration," *Computer Vision and Pattern Recognition Workshops (CVPRW), 2011 IEEE Computer Society Conference on*, pp. 61 - 67, 2011.
- [22] A. Verri and T. Poggio, "Motion Field and Optical Flow: Qualitative Properties," *IEEE Trans. Pattern Analysis and Machine Intelligence*, 11(5), pp. 490{498, May, 1989.
- [23] P. Viola and W. M. Wells, "Alignment by Maximization of Mutual Information," *Intl. J. of Computer Vision*, vol. 24, no. 2, pp. 137-154,, 1997.
- [24] M. Yaman and S. Kalkan, "An iterative adaptive multi-modal stereo-vision method using mutual information," *Journal of Visual Communication and Image Representation*, vol. 26, pp. 115-131, 2015.
- [25] Y. Zhang and K. Qi, "Snake-Search Algorithm for Stereo Vision Reconstruction via Monocular System," presented at the The 5th Annual IEEE Conference on Cyber Technology in Automation, and Control, Intelligent Systems, Shenyang, China, 2015.
- [26] B. Zitová and J. Flusser, "Image registration methods: a survey," *Image and Vision Computing*, vol. 21, pp. 977-1000, 2003.